Investigation of a 3D-Magnetic Flux PMSM with High Torque Density for Electric Vehicles

Hao Chen, *Member, IEEE*, Nabeel A. O. Demerdash, *Life Fellow, IEEE*, Ayman M. EL-Refaie, *Fellow, IEEE*, Youguang Guo, *Senior Member, IEEE*, Wei Hua, *Senior Member, IEEE*, and Christopher H. T. Lee, *Senior Member, IEEE*

***Abstract*—This paper presents an investigation of a 3D-magnetic flux permanent magnet synchronous motor (3D-MF PMSM) used for electric vehicle applications. The investigated 3D-MF PMSM consists of an integrated radial-flux and axial-flux structure. It has two radial-flux air-gaps and two axial-flux air-gaps, as well as a toroidal winding wound stator. The integrated structure helps to concentrate all the flux within the motor to maximize torque production. Moreover, there are no end-windings in this motor and all the stator windings effectively are used in torque production. A comprehensive performance evaluation, in terms of the back-electromotive force, average output torque, cogging torque, torque ripple, flux-weakening capability, etc., of the investigated 3D-MF PMSM is conducted. An interior PMSM is purposely included as a benchmark for comparison. The results show that compared to the benchmark interior PMSM, the original 3D-MF PMSM exhibits significantly improved torque density, higher power factor, and higher efficiency, but suffers from serious cogging torque and torque ripple. Accordingly, a skewed arrangement is introduced to the 3D-MF PMSM. As a result, the cogging torque and torque ripple are significantly reduced.**

***Index Terms*—3D-magnetic flux, electric vehicle, flux-weakening capability, high torque density, permanent magnet synchronous motor (PMSM).**

NOMENCLATURE

AMC	Active material cost.
B_{s0}	Slot opening width.
B_{s1}	Slot body width.
GCD	Greatest common divisor.
H_{irp}	Thickness of the PM on the inner rotor.
H_{iry}	Outer rotor yoke height.
H_{orp}	Thickness of the PM on the outer rotor.
H_{ory}	Outer rotor yoke height.
H_{s0}	Slot opening height.
H_{s1}	Slot body height.
H_{srp}	Thickness of the PM on the side axial rotor.
H_{sry}	Side axial rotor yoke height.
$I_{\max}$	Amplitude of the phase current.
i_d	*D*-axis current.
i_q	*Q*-axis current.
i_{rated}	Rated current.
i_s	Current vector.
i'_s	Equivalent current vector for the integrated right rotor of the skewed 3D-MF PMSM.
k_d	Distribution factor.
k_{fw}	Flux-weakening coefficient.
k_q	Pitch factor.
k_w	Winding factor.
k'_w	Winding factor for the skewed 3D-MF PMSM.
L_{ag}	Air-gap length.
L_d	*D*-axis inductance.
L_q	*Q*-axis inductance.
L_{st}	Axial length of the stator.
L_{tot}	Total axial length.
m_{Cu}	Copper mass.
m_{Fe}	Iron core mass of the rotor.
m_{PM}	PM mass.
m_{SMC}	Soft magnetic composite mass.
N_{cog}	Number of cogging periods per revolution.
N_s	Number of slots.
P	Number of poles.
P_{core}	Core losses of stator and rotor.
P_{cu}	Copper losses.
P_{eddy}	Eddy-current losses in PMs.
P_{fw}	Friction and windage.
P_{out}	Output power.
P_{stray}	Stray losses.
q	Number of slots per pole per phase.
R_{iri}	Inner radius of the inner stator.
R_{oro}	Outer radius of the outer rotor.
R_{si}	Inner radius of the stator.
R_{so}	Outer radius of the stator.
T_{axial}	Torque generated by axial-flux machine part.
$T_{external}$	Torque generated by external radial-flux machine part.
$T_{internal}$	Torque generated by internal radial-flux machine part.
T_{total}	Total torque.
T_{total_left}	Left torque generated by the integrated left rotor.
T_{total_right}	Right torque generated by the integrated right rotor.
y	Coil pitch measured in number of slots.

H. Chen and C. H. T. Lee are with the School of Electrical and Electronic Engineering, Nanyang Technological University, Singapore 639798 (e-mail: hao.chen@ntu.edu.sg, chtlee@ntu.edu.sg).

N. A. O. Demerdash and A. M. EL-Refaie are with the Department of Electrical and Computer Engineering, Marquette University, Milwaukee, WI 53233 USA (email: nabeel.demerdash@marquette.edu; ayman.el-refaie@marquette.edu).

Y. Guo is with the School of Electrical and Data Engineering, University of Technology Sydney, NSW 2007, Australia (email: youguang.guo-1@uts.edu.au).

W. Hua is with the School of Electrical Engineering, Southeast University, Nanjing 210096, China (e-mail: huawei1978@seu.edu.cn).

α_e	Electrical slot-pitch angle.
α_p	Pole embrace.
β	Skew angle.
γ	Current control angle (inner power factor angle).
η	Efficiency.
θ_{cog}	Electrical period of the cogging torque.
ψ_m	PM flux linkage.

I. Introduction

With the ever-increasing concerns on the issues of energy conservation and environmental pollution associated with fossil fuels, conventional vehicles equipped with internal combustion engine are, sooner or later, expected to be replaced by electric vehicles (EVs) [1]. EVs have the potential to offer an ultimate solution for clean-energy personal mobility, especially if they are powered by electrical energy generated from renewable energy sources, such as wind, solar, biofuels, and tidal streams [2].

As the key enabling technology for EVs, electric motors should be designed to have high torque densities to provide high output torque capability for electric launch, hill climbing, as well as acceleration in the low-speed region, and good flux-weakening capability to expand the constant-power speed range in the high-speed region. A variety of electric motors have been used for EV applications. Switched reluctance motors have been recognized to have a considerable potential for EVs, *e.g.*, the Chloride Lucas (a commercialized EV), due to their rugged and simple construction, hazard-free operation, and good torque-speed characteristics. However, they suffer from low torque densities, as well as fairly high torque ripple and acoustic noise [3]. Induction motors are a widely accepted candidate for EVs, *e.g.*, the Tesla Model S, due to their high reliability, low cost, and reduced maintenance. The limitation of induction motors includes low torque density, low power factor, and low efficiency [4]. With the advent of high-energy permanent magnet materials, permanent magnet synchronous motors (PMSMs) have been identified to be the most promising candidates to provide high performance metrics for modern EVs, *e.g.*, the Toyota Prius and Honda Civic, due to the advantages of high torque density, high power density, and high efficiency [5], [6]. Accordingly, a PMSM used for EV applications is investigated in this paper.

Many design variants of PMSMs have been investigated for EV applications, including various stator PM motors, *e.g.*, flux-switching PM motors [7], flux-reversal PM motors [8], and doubly-salient PM motors [9], as well as rotor PM motors, *e.g.*, surface-mounted PMSMs [10] and interior PMSMs [11]. Among them, surface-mounted and interior PMSMs have led the way due to their relatively simple structures and good electromagnetic characteristics. In general, these PMSMs consist of laminated stators housing windings and solid or laminated rotors where PMs are mounted on the surfaces of such rotors or inserted in such rotor cores. High torque density is imperative for electric motors in EV applications, where the motor's volume/weight is often highly constrained [12]. In order to improve the torque density, Niu *et al.* presented a double-stator surface-mounted PMSM, which incorporates the merits of an outer stator with fractional-slot concentrated winding configuration and an inner stator with multi-tooth structure combined into one compact PM motor [13], [14]. It was shown that compared to conventional PMSM counterparts, this motor exhibits improved torque density and efficiency, as well as reduced cogging torque. In [15], Gul *et al.* also presented a double-stator surface-mounted PMSM, which combines an inner-rotor PMSM and an outer-rotor PMSM into a double-stator single-rotor PMSM. It was shown that compared to conventional counterparts, this machine exhibits improved torque density, reduced cost and size. Moreover, the cogging torque of this machine is mitigated by optimizing slot position of both stators with respect to each other. Similarly, in [16], Zhao *et al.* presented a double-stator spoke-type interior PMSM. It was found that compared to a standard PM motor, this motor exhibits significantly improved torque/power density, reduced torque ripple, and improved efficiency. By contrast, Chen *et al.* and Li *et al.* presented a double-rotor PMSM in [17] and [18], respectively. Compared to the double-stator counterparts in [13]-[16], besides the improved torque density, these motors are more suitable for direct-drive operation, which is favorable in EV applications. In addition, Potgieter *et al.* presented a double-rotor PMSM with ring wound windings for direct-drive applications in [19]. It was shown that compared to overlap-winding counterparts, this machine has the advantage of shorter end-windings. Meanwhile, compared to conventional concentrated winding counterparts, this machine exhibits further improved torque density, reduced torque ripple, as well as reduced eddy-current and PM losses.

On the other hand, axial-flux PM machines have shown promising potential for EV applications, due to their high torque density, compact structure with short axial length, and good heat dissipation [20]. In [21], Zhao *et al.* presented a double-stator axial-flux PMSM for traction applications. It was shown that the torque density of this machine is as high as 35.33 Nm/L, which is higher than that of conventional PMSMs in commercialized EVs. In [22], [23], Lu *et al.* presented a six-phase double-stator axial-flux PMSM with detached windings. It was found that compared to conventional winding counterparts, the rotor eddy-current losses of this motor could be reduced by 25% and 75% under normal and fault-tolerant operation, respectively, without sacrificing average output torque. This feature is favourable for safety-critical EV applications. By contrast, Mahmoudi *et al.* and Geng *et al.* presented a double-rotor axial-flux PMSM in [24] and [25], respectively. It should be noted that the torque density has been improved by these aforementioned double-stator or double rotor structures, since they are equivalent to integrating two motors into one. However, pursuing more torque density is an evergreen research highlight in EV applications.

Recently, a hybrid axial-radial flux PM machine with is presented in [26]. This machine combines axial- and radial-flux PM machines into one compact space, which effectively improves the copper utilization of the machine. Moreover, Halbach array PMs are used to achieve a more sinusoidal back-electromotive force (EMF) waveform.

This paper presents a comprehensive investigation of a 3D-MF PMSM for EV applications. The investigated machine consists of an integrated radial-flux and axial-flux structure which has two radial-flux air-gaps and two axial-flux air-gaps,

as well as a toroidal winding wound stator. This compact concept was firstly patented in [27]. This paper brings contributions by comprehensively investigating the performance metrics of the 3D-MF PMSM, conducting the comparison with a benchmark commercialized machine, and quantifying its potential for EV applications. Differing from conventional PMSMs in which end-windings are wasted in terms of torque production, all the windings (wirings) of this machine are used for torque production. In addition, with the significantly extended air-gap areas where the magnetic energy is stored, this machine exhibits remarkably improved torque density. The remainder of this paper is organized as follows: In Section II, the 3D-MF PMSM is designed and investigated. Meanwhile, in order to reduce the cogging torque and torque ripple, a skewed 3D-MF PMSM is also introduced and investigated. In Section III, the performance metrics of the three motors (the benchmark interior PMSM, original 3D-MF PMSM, and skewed 3D-MF PMSM), in terms of back-EMF waveform, average output torque, cogging torque, torque ripple, flux-weakening capability, *etc.*, are comprehensively compared. In Section IV, design aspects including assembling details, as well as thermal and mechanical stress analysis, are provided to demonstrate the feasibility of the investigated 3D-MF PMSM. Finally, Section V is dedicated to the conclusions.

II. 3D-Magnetic Flux PMSM

The investigated 3D-MF PMSM is shown in Fig. 1. This integrated motor consists of four rotors with surface-mounted PMs, *i.e.*, two axial rotors including a left axial rotor and a right axial rotor, two radial rotors including an outer radial rotor and an inner radial rotor. Hence, this machine can be considered as four machines, *i.e.*, two axial-flux machines (a left axial-flux machine and a right axial-flux machine), and two radial-flux machines (an internal radial-flux machine and an external radial-flux machine). It should be noted that both the outer and inner radial rotors are divided into two parts, *i.e.*, a left part and a right part. For the ease of understanding, the left parts of both the outer radial rotor and inner radial rotor, as well as the left axial rotor are formed and named as the "integrated left rotor". By contrast, the right parts of both the outer radial rotor and inner radial rotor, as well as the right axial rotor are formed and named as the "integrated right rotor". A stator wound by toroidal discrete windings without end-windings are adopted. The stator is surrounded by the rotors while the inner rotor sits at the center of the cylindrical structure.

The geometry and the magnetic flux path of the investigated 3D-MF PMSM including both radial-flux part and axial-flux part, are shown in Fig. 2. The main parameters are listed in Table I. As can be seen, differing from conventional 2D-magnetic flux motors which consist of only either a radial- or axial-flux path, this motor consists of both radial- and axial-flux paths. More specifically, as shown in Fig. 2(a), the radial-flux path goes in the direction as follows: the PM on the outer rotor marked as red color → the stator tooth → the PM on the inner rotor marked as red color → the inner rotor yoke → the PM on the inner rotor marked as yellow color → the stator tooth → the PM on the outer rotor marked as yellow color → the outer rotor yoke → the PM on the outer rotor marked as red color. By contrast, the axial-flux setup path goes in the direction as follows: the PM on the left axial rotor marked as red color → the stator tooth → the PM on the right axial rotor marked as red color → the right axial rotor yoke → the PM on the right axial rotor marked as yellow color → the stator tooth→ the PM on the left axial rotor marked as yellow color → the left axial rotor yoke → the PM on the left axial rotor marked as red color. In this way, both the radial- and axial-flux paths form closed loops. This is the so-called "3D-magnetic flux PMSM". It should be noted that differing from the conventional laminated, the stator material of the investigated 3D-MF PMSM should be a solid magnetic material with an isotropic ferromagnetic behaviour and homogenous magnetic characteristic in both the radial and axial directions, which is able to carry both the radial- and axial-flux. Accordingly, the soft magnetic composite (SMC) of Hoganas/Somaloy is used as the stator core material of the presented 3D-MF PMSM, which could be produced by either advanced compaction and later matching technologies [28], [29], or advanced 3D printing technologies. The B-H curve and the core losses characteristics of the Somaloy 700HR used in this paper are shown in Fig. 3(a) and (b), respectively. It should be also noted that there is a 2 mm small airgap between the "integrated left rotor" and the "integrated right rotor", which is potentially used for introducing a phase displacement (the skew angle, β) between the "integrated left rotor" and the "integrated right rotor".

The magnetic flux vector distributions of the presented 3D-MF PMSMs are shown in Fig. 4. Two different arrangements, *i.e.*, original arrangement and skewed arrangement, are presented. The original 3D-MF PMSM aligns the "integrated left rotor" and the "integrated right rotor" with each other. By contrast, a skewed arrangement of the "integrated left rotor" and the "integrated right rotor" is adopted in the skewed 3D-MF PMSM, as shown in Fig. 4(b). The skew angle, β, between the "integrated left rotor" and the "integrated right rotor" is equal to 3.75° (mech. deg.) for the purpose of suppressing the cogging torque and torque ripple, which will be elaborated in detail in Section IV-C.

As can be seen from Fig. 1 to Fig. 4, theoretically, all of the magnetic fields generated by the toroidal windings are involved in energy conversion (torque production). By contrast, conventional motors consist of wasted end-windings [refer to Fig. 2(a)], which produce no torque but lead to the increment of volume, weight, cost, as well as losses. On the other hand, in principle, the electromagnetic torque produced by the interaction of the two magnetic fields from the current-excited stator and the PM-excited rotating rotor, is proportional to the change in the stored magnetic energy in the air-gap. The investigated 3D-MF PMSM consists of two radial-flux air-gaps and two axial-flux air-gaps, which significantly extends the air-gap area. Moreover, all magnetic flux is concentrated within this motor due to the unique 3D-MF structure (refer to Fig. 2). Hence, this motor is expected to have the advantage of high torque density. In addition, the toroidal concentrated winding configuration is amiable to have a higher slot fill factor, which is expected to further improve the torque density.

The current vector diagram is shown in Fig. 5. As can be seen, for the original 3D-MF PMSM and the integrated left part of the skewed 3D-MF PMSM, the current diagram is similar to

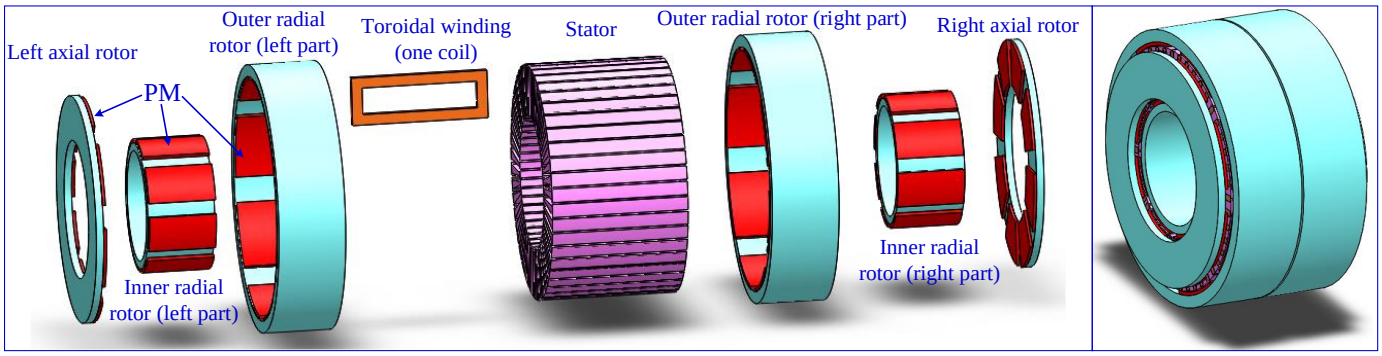

(a) (b)

Fig. 1. The investigated 3D-MF PMSM. (a) Exploded view, and (b) Assembled view.

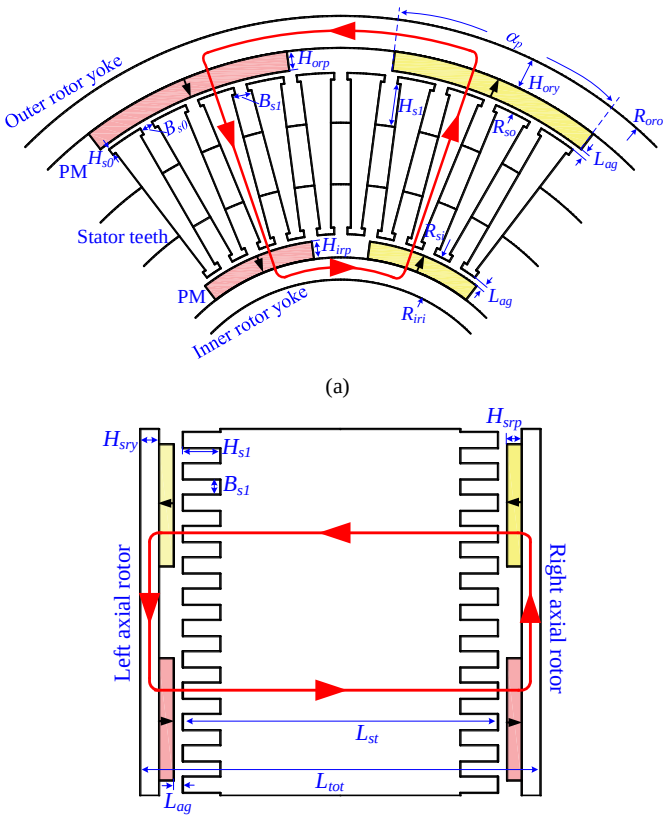

(a)

(b)

Fig. 2. Geometry and Magnetic flux path of the 3D-MF PMSM. (a) Radial-flux part. (b) Axial-flux part.

that of conventional surface-mounted PMSMs, while for the integrated right part of the skewed 3D-MF PMSM, there is an additional angle of ($\beta \cdot P/2$) in electrical degrees due to the skewed arrangement with the skew angle, β, added to the current control angle, γ. It should be noted that the reluctance torque of surface-mounted PMSMs is negligible, due to the almost equal magnitudes of L_d and L_q. The same applies to the investigated 3D-MF PMSM, since the original 3D-flux PMSM shares the same operation principle with surface-mounted PMSMs. Hence, the electromagnetic torque can be expressed for the original 3D-MF PMSM as follows:

$$T_{total} = 2 \times T_{axial} + T_{internal} + T_{external} = (3/2) \cdot (P/2) \cdot \psi_m \cdot i_q = (3/2) \cdot (P/2) \cdot \psi_m \cdot (I_{\max} \cdot \cos\gamma) \quad (1)$$

By contrast, for the skewed 3D-MF PMSM, the total torque, T_{total}, is a combination of the left torque generated by the integrated left rotor, T_{total_left}, and the right torque generated by the integrated right rotor, T_{total_right}, which can be expressed as:

TABLE I
MAIN PARAMETERS OF THE INVESTIGATED 3D-MF PMSM

Basic parameters			
Number of stator slots	48		
Number of poles	8		
Base speed (r/min)	1200		
Amplitude of rated phase current (A)	150		
Current density (A/mm^2)	12.49		
Slot fill factor (%)	48.13		
Material of PM	N36Z_20 (NdFeB)		
Material of rotor core	M19_29G		
Material of stator core	Somaloy 700HR		
Geometry parameters			
R_{oro} (mm)	134.62	H_{orp} (mm)	3.50
R_{so} (mm)	118.39	H_{irp} (mm)	4.00
R_{si} (mm)	68.05	H_{srp} (mm)	3.00
R_{iri} (mm)	55.32	α_p	0.73
L_{tot} (mm)	159.77	L_{aq} (mm)	0.73
L_{st} (mm)	137.31	B_{s0} (mm)	1.93
H_{ory} (mm)	12.00	H_{s0} (mm)	1.02
H_{iry} (mm)	8.00	B_{s1} (mm)	6.09
H_{sry} (mm)	7.50	H_{s1} (mm)	10.61

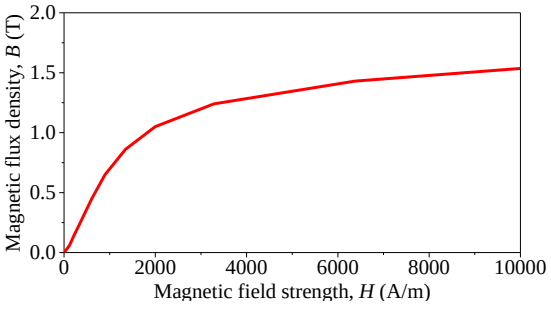

(a)

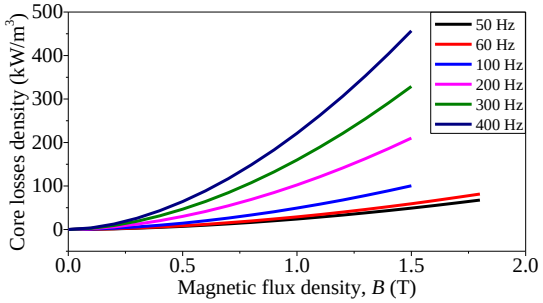

(b)

Fig. 3. Material properties of the Somaloy 700HR. (a) B-H curve, and (b) Core losses characteristics.

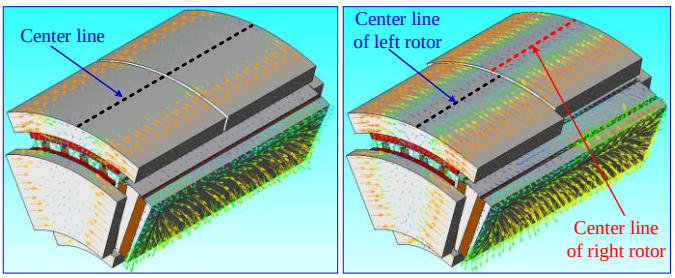

(a) (b)

Fig. 4. Magnetic flux vector distributions of the 3D-MF PMSMs. (a) Original 3D-MF PMSM, and (b) Skewed 3D-MF PMSM.

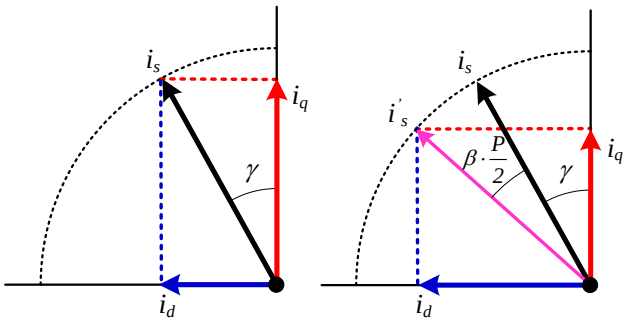

(a) (b)

Fig. 5. Current vector diagram. (a) Original 3D-MF PSMM and the integrated left part for the skewed 3D-MF PMSM. (b) The integrated right part for the skewed 3D-MF PMSM.

$$\left.\begin{aligned} T_{total} &= T_{total\_left} + T_{total\_right} \\ T_{total\_left} &= \frac{1}{2}\left(\frac{3}{2}\cdot\frac{P}{2}\cdot\psi_m \cdot i_{q\_left}\right) \\ &= \frac{1}{2}\left[\frac{3}{2}\cdot\frac{P}{2}\cdot\psi_m \cdot \left(I_{\max}\cdot\cos\gamma\right)\right] \\ T_{total\_right} &= \frac{1}{2}\left(\frac{3}{2}\cdot\frac{P}{2}\cdot\psi_m \cdot i_{q\_right}\right) \\ &= \frac{1}{2}\left\{\frac{3}{2}\cdot\frac{P}{2}\cdot\psi_m \cdot \left[I_{\max}\cdot\cos\left(\gamma+\beta\cdot\frac{P}{2}\right)\right]\right\} \end{aligned}\right\} \quad (2)$$

As can be seen, even though only one current vector, i_s, exists in the field-oriented control, an equivalent current vector, i_s', instead of the current vector, i_s, behaves to generate the output torque for the integrated right part of the skewed 3D-MF PMSM, due to the misalignment/skew angle, β.

III. Performance Comparison

In order to comprehensively evaluate the performance of the investigated 3D-MF PMSMs, a quantitative comparison of the investigated motors and a benchmark PMSM is conducted in this section. The interior PMSM used in 2004 Toyota Prius EV is adopted to serve as the benchmark for this study, as shown in Fig. 6. The dimensional specifications and experimental results of the interior PMSM are obtained from ref. [30] and [31]. For a fair comparison, the 3D-MF PMSMs share the same volume, rated current, and current density as the benchmark interior PMSM. These designs are considered at the temperature of 95 °C with a typical liquid-cooling system [32].

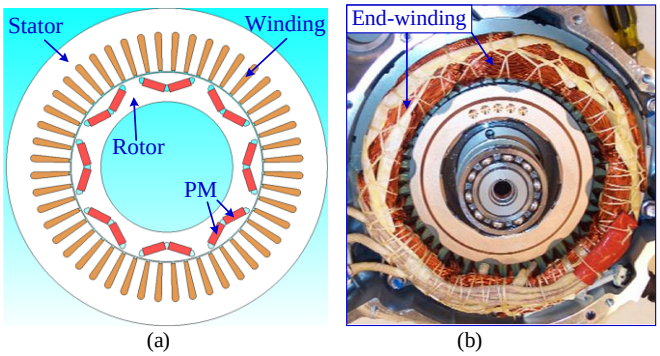

(a) (b)

Fig. 6. Benchmark interior PMSM. (a) Structure. (b) Prototype [30].

A. Winding Configuration

Since the interior PMSM and the 3D-MF PMSMs share the same slot/pole combination, *i.e.*, 48-slot /8-pole, they have the same star of slots, as shown in Fig. 7. Hence, they have the same electrical slot-pitch angle in electrical degrees as follows:

$$\alpha_e = P\cdot 180°/N_s = 30°e \quad (3)$$

They also have the same winding distribution factor as follows:

$$k_d = \sin\left[q\cdot(\alpha_e/2)\right]/\left[q\cdot\sin(\alpha_e/2)\right] = 0.9659 \quad (4)$$

where q=2 is the number of slots per pole per phase. Accordingly, the winding configurations of the three motors are shown in Fig. 8. For the interior PMSM with overlapping distributed windings, the pitch factor is as follows:

$$k_q = \sin(y\cdot\alpha_e/2) = 1 \quad (5)$$

where y=6 is the coil pitch measured in number of slots [refer to Fig. 8(a)]. For the 3D-MF PMSMs with non-overlapping toroidal windings, since the four lateral edges of the rectangle-shaped toroidal winding coil can link the same flux as a full-pitched coil, the winding pitch factor is, k_q=1 [33]. Hence, the original 3D-MF PMSM has the same winding factor as the benchmark interior PMSM as follows:

$$k_w = k_d \cdot k_q = 0.9659 \quad (6)$$

For the skewed 3D-MF PMSM, since the integrated right rotor is shifted by an angle of β with respect to the integrated left rotor, the left winding part and the right winding part have a phase shift of $\beta\cdot(P/2)$ in electrical degrees. Hence, the winding factor for the skewed 3D-MF PMSM is computed based on that of the original 3D-MF PMSM as follows:

$$k_w' = k_w\cdot\cos\left[\beta\cdot(P/2)/2\right] = 0.9576 \quad (7)$$

B. Magnetic Field

The no-load flux density distribution results of the two 3D-MF PMSMs at the initial rotor position where the flux linkage of phase-A reaches the maximum value, are shown in Figs. 9(a) and (b), respectively. As can be seen, a reasonable level of saturation is maintained in both stator teeth and rotor yoke for both of the two motors. The air-gap flux density profiles of the two 3D-MF PMSMs as well as the benchmark interior PMSM under no-load condition are shown in Fig. 10. It should be noted that the results for the original 3D-MF PMSM are from the integrated left rotor, while those for the skewed 3D-MF PMSM are from the integrated right rotor. As can be

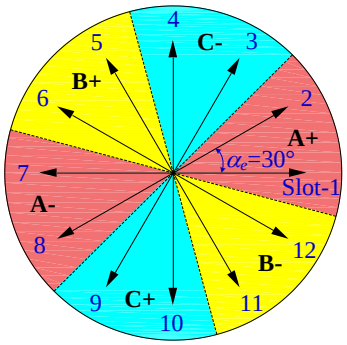

Fig. 7. Star of slots.

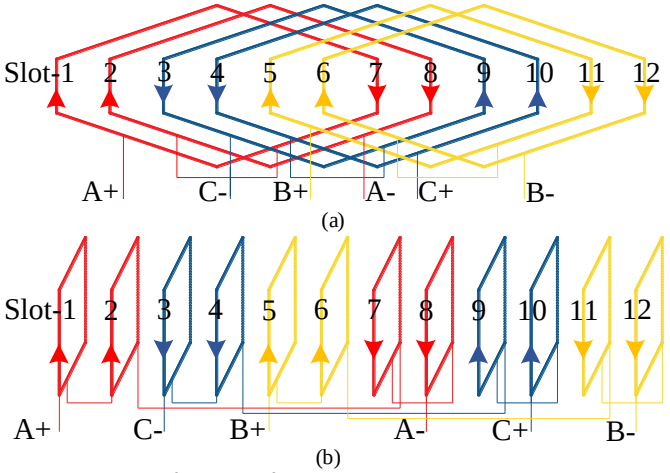

Fig. 8. Winding configurations for one basic repeating unit machine (12 slots). (a) Interior PMSM, and (b) 3D-MF PMSMs.

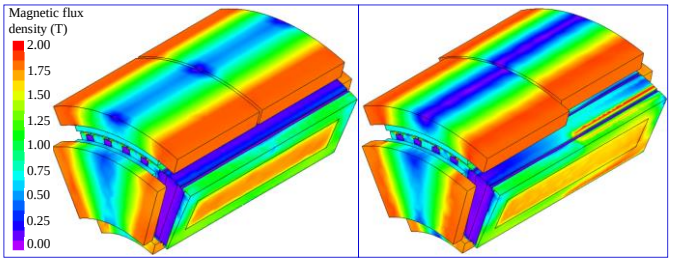

Fig. 9. No-load magnetic flux density distribution of the two 3D-MF PMSMs. (a) Original, and (b) Skewed.

seen, the fundamental component amplitudes of the air-gap flux density for the two 3D-MF PMSMs are slightly lower than that of the interior PMSM. This is because the stator core of the 3D-MF PMSMs works as the magnetic paths for both radial- and axial-flux, which makes it be prone to be at a higher saturation level (refer to Fig. 9), while the stator core of the interior PMSM only works as the magnetic paths for radial-flux. In the meantime, the amplitudes of these harmonic orders of the original 3D-MF PMSM are almost the same as the corresponding components of the skewed 3D-MF PMSM, *e.g.*, harmonic orders in the outer air-gap of the original 3D-MF PMSM vs. harmonic orders in the outer air-gap of the skewed 3D-MF PMSM. These results indicate that the skewed arrangement in the skewed 3D-MF PMSM has negligible effect on the main magnetic flux. It should be noted that the increased higher order harmonics may lead to torque ripple, vibration and acoustic noise, iron losses, and PM eddy-current losses.

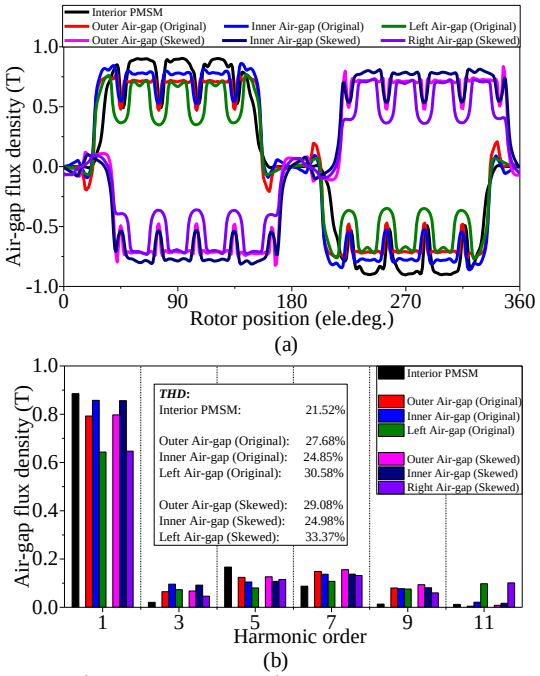

Fig. 10. Air-gap flux density. (a) Waveform, and (b) Harmonic spectrum.

Techniques to reduce the higher order harmonics, *e.g.*, unequal thickness PMs and Halbach array PMs, will be investigated in future work.

The no-load back-EMF waveforms at the rated speed of 1200 r/min and their corresponding harmonic spectrum, are shown in Fig. 11. As can be seen, compared to the interior PMSM, the fundamental components of the back-EMF waveform of the 3D-MF PMSMs are significantly improved, even though the air-gap flux density of the 3D-MF PMSMs is slightly lower than that of the interior PMSM. This is due to the fact that the air-gap area which functions for energy conversion is significantly extended in the 3D-MF PMSMs. This feature indicates that the 3D-MF PMSMs are expected to have a high output torque/power. On the other hand, compared to the original 3D-MF PMSM, the total harmonic distortion (*THD*) of the skewed 3D-MF PMSM is significantly reduced from 10.72% to 6.60%, with a little sacrifice of the fundamental component amplitude, which is favourable for the reduction of torque ripples.

C. Torque Characteristics in the Low-Speed Region

In the low-speed region, motors for EV applications are expected to have the following features: 1) Low cogging torque, T_{cog}, and torque ripple, T_{rip}, to suppress acoustic noise and vibrations; 2) Sufficient average output torque, T_{avg}, to provide enough driving force; 3) Good overload capability for hill-climbing and acceleration operations; and 4) High efficiency, η, to save the limited energy from the battery. Accordingly, these aforementioned performance metrics of the three motors are investigated in detail.

The number of cogging periods per revolution in PMSMs, N_{cog}, can be expressed as follows:

$$N_{cog} = N_s \cdot P / GCD(N_s, P) \tag{8}$$

The electrical period of the cogging torque, θ_{cog} is as follows:

$$\theta_{cog} = \pi \cdot P / N_{cog} \tag{9}$$

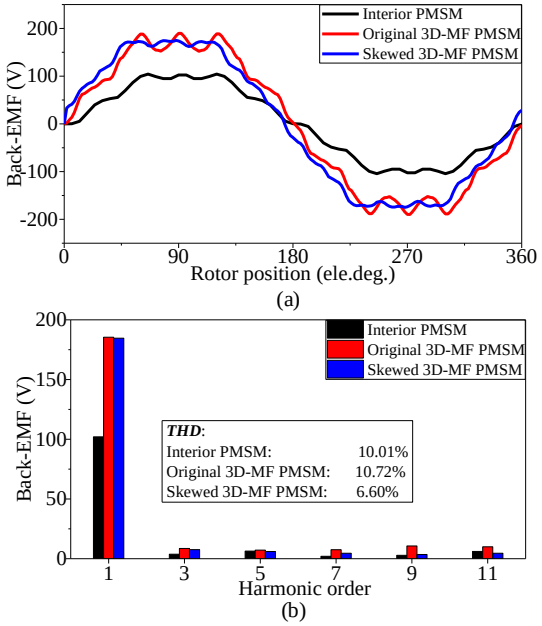

Fig. 11. Back-EMF. (a) Waveform, and (b) Harmonic spectrum.

Hence, for the 48-slot/8-pole PM machines investigated in this paper, N_{cog} = 48, θ_{cog} = 30° in electrical degrees. The cogging torque waveform with two periods of the original 3D-MF PMSM is shown in Fig. 12(a). As can be seen, the cogging torque waveform of the integrated left rotor is overlapping with that of the integrated right rotor, and the total cogging torque is almost double of that of the former or the latter.

If the integrated left rotor and the integrated right rotor are skewed so that the cogging torque of the integrated right rotor has a phase shift of $(2n\text{-}1)\cdot 180°$ (elec. deg.) in cogging periods with respect to the integrated left rotor, the total cogging torque can be minimized. Hence, the skew angle, β, in mechanical radians can be expressed as follows:

$$\beta = \left[(2n-1)\pi / (2\pi/\theta_{cog})\right] / (P/2) = (2n-1)\pi/48 \quad n=1,2,3... \quad (10)$$

As can be seen from eq. (7) and eq. (10), with n increasing, the skew angle, β, will increase step by step while the winding factor will decrease, which means the output torque will be reduced. Hence, in order to reduce the cogging torque and maintain the average output torque as much as possible, n is set as 1. Accordingly, the skew angle, $\beta = 3.75°$ (mech. deg.).

The cogging torque waveform of the skewed 3D-MF PMSM is shown in Fig. 12(b). As can be seen, compared to the original 3D-MF PMSM, the cycles/frequency of the total cogging torque in the skewed 3D-MF PMSM are doubled, while the amplitude of the total cogging torque is significantly reduced by 75.04%, *i.e.*, from 38.06 Nm to 9.50 Nm.

The torque profile at the rated current of 150 A is shown in Fig. 13(a). As can be seen, compared to the benchmark interior PMSM, the average torque, T_{avg}, of the original 3D-MF PMSM is significantly improved by 34.37%, *i.e.*, from 239.03 Nm to 321.19 Nm. However, the torque ripple, T_{rip}, of the original 3D-MF PMSM is very large. Fortunately, with the skewed arrangement mentioned above, the torque ripple, T_{rip}, of the skewed 3D-MF PMSM is significantly reduced by 51.96%, *i.e.*, from 30.39% to 14.60%, with a little sacrifice of the average torque (< 3.5%), compared to the original 3D-MF PMSM. It

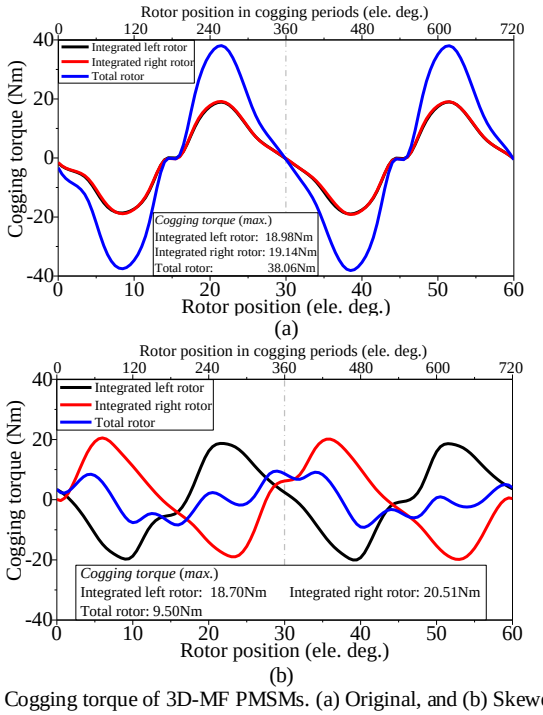

Fig. 12. Cogging torque of 3D-MF PMSMs. (a) Original, and (b) Skewed.

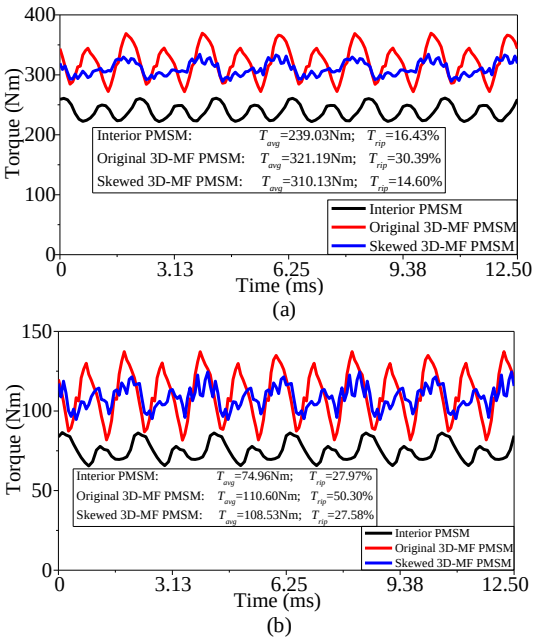

Fig. 13. Torque profiles. (a) Rated current condition (150 A), and (b) Low current condition (50 A).

should be noted that the current density of the three motors at the rated current of 150 A is as high as 12.49 A/mm^2. By contrast, the torque profile at a low current of 50 A where the current density is 4.16 A/mm^2, is shown in Fig. 13(b). As a result, similar conclusions can be drawn. More specifically, compared to the benchmark interior PMSM, the average torque, T_{avg}, of the original 3D-MF PMSM is significantly improved by 47.55%, *i.e.*, from 74.96 Nm to 110.60 Nm, while the torque ripple, T_{rip}, of the skewed 3D-MF PMSM is much lower than that of the original 3D-MF PMSM (27.58% vs. 50.30%), with a little sacrifice of the average torque (<1.9%). It should be noted that the current control angle, γ=43° and γ=28° are used for the

interior PMSM with the MTPA control mode at current values of 150A and 50A, respectively, while γ=0° for the two 3D-MF PMSMs is used with the $i_d = 0$ control mode.

The average torque and torque ripple versus input current profiles are shown in Figs. 14(a) and (b), respectively. These results can help to estimate the overload capability of the investigated motors. As can be seen, with the phase current amplitude increasing, the average torque of the two 3D-MF PMSMs is almost linearly increasing, while the benchmark interior PMSM suffers more from magnetic saturation in the region above 150 A. Moreover, all the torque ripples of the skewed 3D-MF PMSM are significantly reduced compared to the original 3D-MF PMSM. Furthermore, the torque ripples from the skewed 3D-MF PMSM are comparable and even lower than those of the benchmark interior PMSM.

The torque versus current control angle of the three investigated motors at the rated current is shown in Fig. 15. As can be seen, the maximum torque of the benchmark interior PMSM is located at a current control angle equal to 43°, while the maximum torque of the two 3D-MF PMSMs is located near a current control angle equal to 0°. These results indicate that the reluctance torque of the interior PMSM is notable and the MTPA control mode should be used below the base speed, while the reluctance torque of the two 3D-MF PMSMs is negligible and $i_d = 0$ control mode is valid below the base speed.

A breakdown of the loss components of the three motors under rated condition is shown in Fig. 16. The efficiency, η, is calculated as follows:

$$\eta = \left[P_{out} / (P_{out} + P_{cu} + P_{eddy} + P_{core} + P_{fw} + P_{stray}) \right] \cdot 100\% \quad (11)$$

It should be noted that both the radial-flux and axial-flux contribute to the core losses since the solid SMC stator carries both the radial-flux and axial-flux. The friction and windage losses, P_{fw}, of the 3D-MF PMSMs are estimated as the same as that of the benchmark interior PMSM, while the stray losses are assumed to be 1% of the output power [34], [35]. As can be seen, compared to the 3D-MF PMSMs, the PM eddy-current losses, P_{eddy}, of the interior PMSM are negligible, since the PMs are inserted in the rotor and relatively far away from the air-gap. The core losses, P_{core}, of the two 3D-MF PMSMs are much higher than that of the interior PMSM, since solid SMC material is used in the stator of the 3D-MF PMSMs, while laminated sheets are used in the interior PMSM. In the meantime, the PM eddy-current losses, P_{eddy}, and the core losses, P_{core}, of the skewed 3D-MF PMSM are slightly higher than those of the original 3D-MF PMSM. Moreover, it is interesting to note that the efficiency, η, of the two 3D-MF PMSMs are improved compared to the benchmark interior PMSM.

D. Flux-Weakening Capability in the High-Speed Region

The flux-weakening capability is of particular importance for EV applications, since it determines loading capability and speed range in the high-speed region.

The flux-weakening characteristics including torque and power versus speed under current and voltage limits are shown in Fig. 17. It should be noted that the interior PMSM is controlled by the MTPA control mode below the base speed, and flux-weakening control mode above the base speed. By

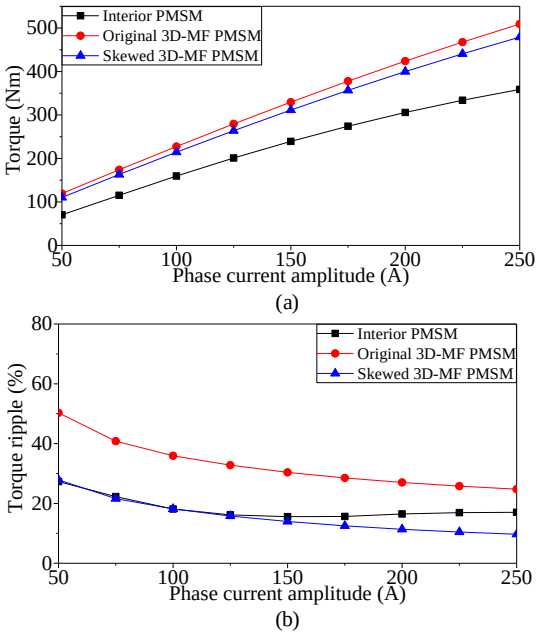

Fig. 14. Torque characteristics with phase current amplitude. (a) Average torque, and (b) Torque ripple.

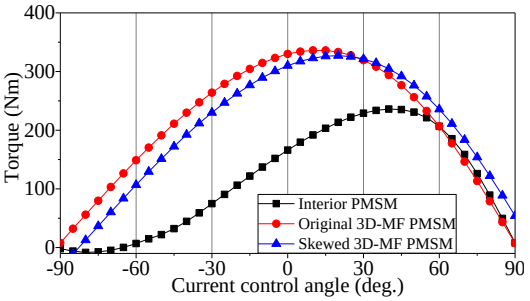

Fig. 15. Torque versus current control angle.

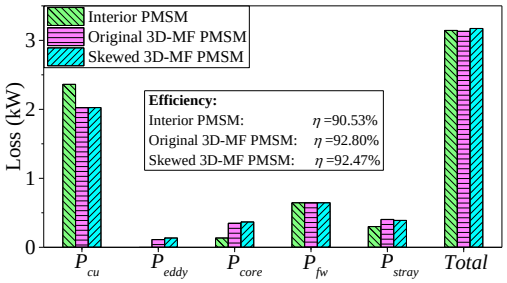

Fig. 16. Loss components.

contrast, the 3D-MF PMSMs are controlled by the $i_d = 0$ control mode below the based speed, and flux-weakening control mode above the base speed. It should be also noted that the results for the skewed 3D-MF PMSM with a variable skew angle, β, are also added. The skewed 3D-MF PMSM with the skew angle, β=0° is the same as the original 3D-MF PMSM, while other skew angle values are selected based on eq. (10) in order to minimize the cogging torque, more specifically, $\beta = (2n\text{-}1) \times 3.75°$ in mechanical degrees, where n = 1, 2, 3,… As can be seen, the original 3D-MF PMSM has a limited constant power-speed range (CPSR), while the skewed 3D-MF PMSM exhibits extended CPSR. Moreover, if the skew angle, β, can be appropriately adjusted with the speed increasing in the high-speed region, the CPSR of the skewed 3D-MF PMSM can

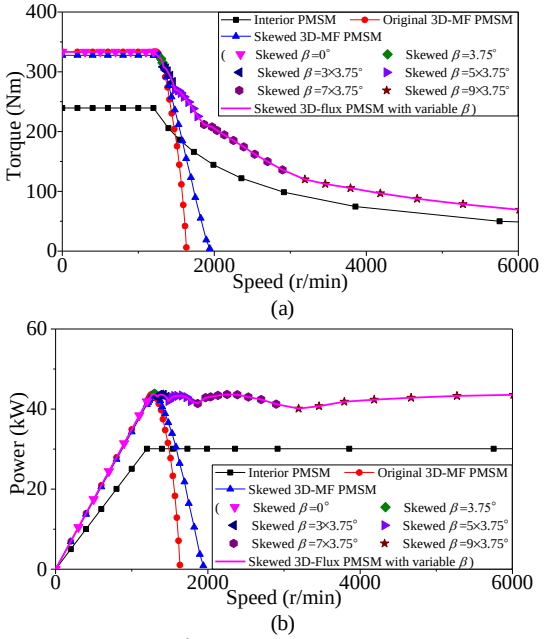

Fig. 17. Flux-weakening performance. (a) Torque vs. speed, and (b) Power vs. speed.

be further extended so that it can be fully weakened as the benchmark interior PMSM does (refer to the results with pink line). This is due to the fact that with the skew angle, β, increasing, the total flux linkage is reduced with the compensation act of the integrated left rotor and the integrated right rotor, which would enhance the flux-weakening capability. The adjustable skew angle can be realized by a mechanical phase displacement strategy, which has been reported in [36]. In order to enable the two rotating parts, *i.e.*, the "integrated left rotor" and the "integrated right rotor", be free to have a phase displacement with respect to the motor shaft, a rotor hub is rigidly mounted on the motor shaft and it supports the two rotating parts through bearings. This rotor hub also supports the shaft of a cam-spring governor that acts on a treadle lever, which is schematically depicted in Fig. 18. The spring of the cam-spring governor is constrained to the hub, while the treadle lever is being rigidly connected to the "integrated right rotor". The equilibrium position of the cam-spring governor is determined by the balance between the centrifugal force acting on the cam and the reaction force exerted by the spring. The original position without phase displacement, *i.e.*, $\beta = 0°$, is shown in Fig. 18(a). When the centrifugal force acting on the cam exceeds the reaction force exerted by the spring, the cam will rotate and a new equilibrium position is found, which results in a skew angle, $\beta (\beta \neq 0°)$, between the "integrated left rotor" and the "integrated right rotor" of the investigated 3D-MF PMSM, as shown in Fig. 18(b).

The efficiency map results are shown in Fig. 19. They are calculated using FEA method with 1282 and 2886 operating points equidistantly distributed throughout the torque-speed plane for the interior PMSM and the 3D-MF PMSM, respectively. As can be seen, the high-efficiency area of the 3D-MF PMSM is larger than that of the interior PMSM. For example, the area with efficiency ≥90% of the 3D-MF PMSM is much larger than that of the interior counterpart. It is more interesting to note that the high-efficiency area of the interior

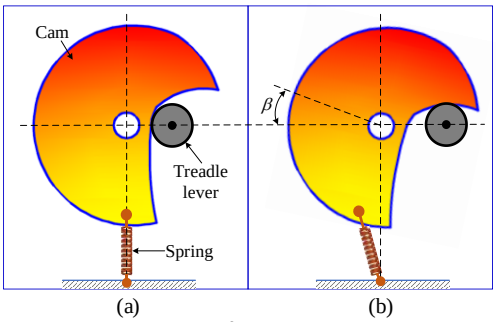

Fig. 18. Schematic representation of a cam-spring governor acting on treadle lever. (a) Original position without phase displacement, and (b) Position with phase displacement.

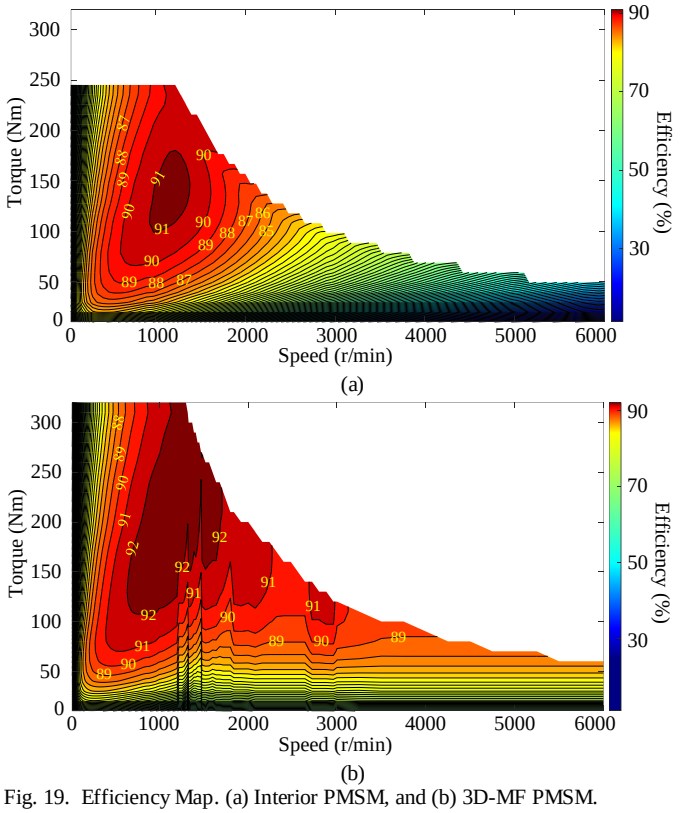

Fig. 19. Efficiency Map. (a) Interior PMSM, and (b) 3D-MF PMSM.

PMSM is located in the relatively low-speed high-torque region, while in the high-speed low-torque region (flux-weakening region), the efficiency is relatively low, as shown in Fig. 19(a). By contrast, the high-efficiency area of the 3D-MF PMSM is extended to the high-speed low-torque region, as shown in Fig. 19(b). Hence, the 3D-MF PMSM is more suitable for EV/traction applications where high efficiency is preferred for both low- and high-speed regions. The unusual form of the efficiency map of the 3D-MF PMSM may be due to the fact that calculating the losses and efficiency for such a large amount of operating point is challenging, and the skew angle, β, will be changing in different region of the torque-speed plane.

E. Results Analysis and Discussion

In order to comprehensively evaluate the presented 3D-MF PMSMs, the key performance metrics of the three investigated motors are summarized and compared in Table II, where the machine's active material cost (AMC) is as follows:

TABLE II
PERFORMANCE COMPARISON OF THE THREE INVESTIGATED MOTORS

	Interior PMSM	Original 3D-MF PMSM	Skewed 3D-MF PMSM
Mass of PM (kg)	1.24	4.06	4.06
Mass of copper (kg)	6.80	4.56	4.56
Mass of stator core (kg)	19.25	23.64	23.64
Mass of rotor core (kg)	5.42	16.55	16.55
Total mass (kg)	32.71	48.81	48.81
Total cylindrical volume (L)	7.56	7.56	7.56
Number of turns/phase	72	64	64
Winding factor, k_w	0.9659	0.9659	0.9576
Phase resistance, (ohm)	0.07	0.06	0.06
Self-inductance, L_{AA} (mH)	2.44	0.83	0.82
Mutual-inductance, L_{AB} (mH)	0.69	0.26	0.26
D-axis inductance, L_d (mH)	1.54	0.99	0.99
Q-axis inductance, L_q (mH)	3.11	1.18	1.15
PM flux linkage, ψ_m (Wb)	0.205	0.359	0.346
Amplitude of back-EMF (V)	102.02	185.43	184.61
THD of back-EMF (%)	10.01	10.72	6.60
Power factor, P_f	0.765	0.905	0.904
Cogging torque, T_{cog} (Nm)	1.85	38.06	9.50
Average torque, T_{av} (Nm)	239.03	321.19	310.13
Torque ripple, T_{rip} (%)	16.43	30.39	14.60
Copper losses (W)	2363	2025	2025
Core losses (W)	135.39	347.91	367.46
PM eddy-current losses (W)	0.51	112.84	134.94
Output power (kW)	30.03	40.36	38.97
Efficiency (%)	90.53	92.80	92.47
Torque density (Nm/L)	31.62	42.49	41.02
Torque/PM mass (Nm/kg)	192.77	79.11	76.39
Power density (kW/L)	3.97	5.34	5.15
Active material cost	74.83	245.87	245.87
Flux-weakening capability, k_{fw}	Fully weakened	1.71	1.75

$$\mathrm{AMC} = 24 \cdot m_{PM} + 5 \cdot m_{SMC} + 3 \cdot m_{Cu} + 1 \cdot m_{Fe} \qquad (12)$$

As can be seen, with the same volume, compared to the benchmark interior PMSM, the two 3D-MF PMSMs show significantly improved torque density, higher power factor, and higher efficiency, but higher PM content and AMC. Techniques to reduce the PM content and AMC, *e.g.*, Halbach array technique, reduced or non-rare-earth PM material, and an interior PM version of the investigated 3D-MF PMSM which relies on more reluctance torque, will be investigated in future work. Even though the cogging torque and torque ripple of the original 3D-MF PMSM are serious, the skewed 3D-MF PMSM exhibits significantly reduced cogging torque and torque ripple. On the other hand, although the CPSR of the two 3D-MF PMSMs is limited, the CPSR is extended with the skewed arrangement of the skewed 3D-MF PMSM compared to the original 3D-MF PMSM. Moreover, the CPSR of the skewed 3D-MF PMSM can be further extended so that it can be fully weakened as the benchmark interior PMSM does if the skew angle, β, can be appropriately adjusted.

IV. DESIGN ASPECTS OF THE INVESTIGATED 3D-MF PMSM

In order to provide researchers and engineers with better understanding of the assembling details of the 3D-MF PMSM, the assembly of the 3D-MF PMSM are shown in Fig. 20. It should be noted that there is a gap between the axial rotor and the outer rotor, which is used for holding the stator through the 24 rivets and the stator supporter as shown in Fig. 20(a). More specifically, the outer diameter of the axial rotor is smaller than the inner diameter of the outer rotor. This gap could be also used for drawing out lead wires, as well as for the end connection of the cooling system. This motor can fit into electric vehicles through the shaft, as described in [30].

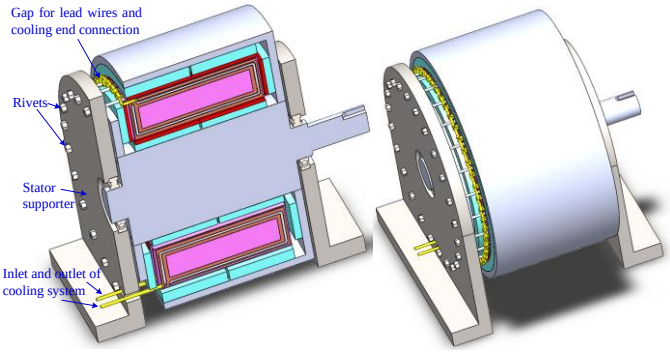

(a) (b)

Fig. 20. Assembly of the 3D-MF PMSM. (a) Section View, and (b) Assembly.

In conventional liquid-cooled electric machines including the benchmark interior PMSM, the cooling jacket is at the stator outer bore, which is referred to as "indirect cooling systems", since the cooling system doesn't directly connect to the windings [37]. By contrast, a "direct cooling system" is designed for the investigated 3D-MF PMSM. As can be seen from Fig. 20, the liquid-cooling tube is directly inserted into the middle hollow area of the toroidal discrete concentrated winding. "Direct cooling systems" have been gaining interest since they can dissipate the heat generated from windings more directly and effectively [38], [39]. It should be noted that with the "direct cooling system", the slot utilization factor of the investigated 3D-MF PMSM would be 58.57% [(copper area + cooling tube area)/slot area] due to the additional ϕ3 mm cooling tube, which is still lower than the slot utilization factor of 70% reported for toroidal windings in [19]. Hence, the cooling system design is practical.

The thermal distribution plots of the 3D-MF PMSM under rated-load condition without and with the cooling system are shown in Fig. 21. As can be seen from Fig. 21(a), without the cooling system, the maximum temperature of this motor is as high as 209.77 ℃. By contrast, with the cooling system [see Fig. 21(b)], the maximum temperature of this motor is reduced to 118.15 ℃, which is lower than the temperature limit of the wire insulation and slot insulation, *i.e.*, 180 ℃ and 180 ℃, respectively. Hence, the cooling system works effectively.

In order to ensure safe operation of the investigated 3D-MF PMSM under high-speed condition, a rotor supporter and retaining sleeves (0.35mm stainless steel) for the PMs on the inner rotor, the left axial rotor, and the right axial rotor are adopted, as shown in Fig. 22(a). A detailed steady-state structural FEA stress analysis is carried out in ANSYS/ Workbench under steady-state maximum speed of 6000 r/min, as shown in Fig. 22(b). The Von-Mises stress results are listed in Table III. As can be seen, all the Von-Mises stresses on the rotor parts are far less than the yield strength. Hence, the rotor of the investigated 3D-MF PMSM has the capability of long-term safe/stable operation.

V. CONCLUSION

In order to improve the torque/power density of the electric motors for EV applications, a 3D-MF PMSM was investigated

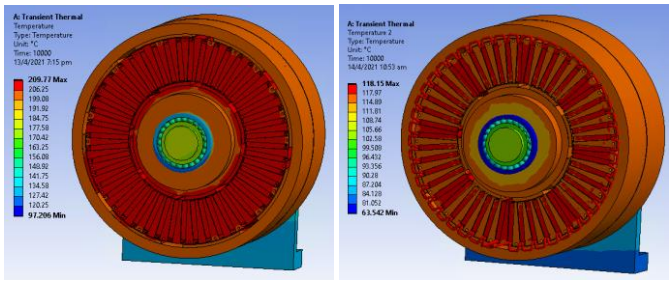

(a) (b)

Fig. 21. Thermal distribution of the 3D-MF PMSM under rated-load condition. (a) Without the cooling system. (b) With the cooling system.

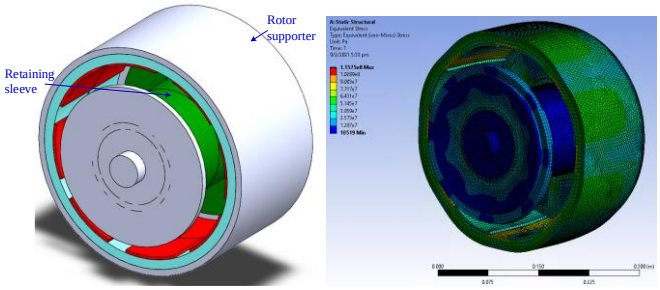

(a) (b)

Fig. 22. (a) Retaining sleeve and rotor supporter for the rotor. (b) Von-Mises stress throughout the rotor structure.

TABLE III
VON-MISES STRESS OF THE ROTOR STRUCTURE

	Yield strength (MPa)	Von-Mises stress (MPa)
Retaining sleeve	200	84.82
PMs	200	97.21
Rotor core	350	115.75
Rotor supporter	335	68.2

in this paper. This motor consists of an integrated radial-flux and axial-flux structure with two radial-flux air-gaps and two axial-flux air-gaps, as well as a toroidal winding wound stator. Compared to a benchmark interior PMSM, the torque density of this motor is significantly improved, due to the significantly extended air-gap area where the magnetic energy is stored, but at the expense of higher PM content and more complicated structure. Meanwhile, an unalignment design is presented in order to reduce the cogging torque and torque ripple. As a result, compared to the benchmark interior PMSM, both of the two 3D-MF PMSMs show significantly improved torque density, higher power factor, and higher efficiency. On the other hand, even though the CPSR of the two 3D-MF PMSMs is limited, the CPSR is extended with the skewed arrangement of the skewed 3D-MF PMSM, compared to the original 3D-MF PMSM. Moreover, the CPSR of the skewed 3D-MF PMSM can be further extended so that it can be fully weakened as the benchmark interior PMSM does if the skew angle, β, can be appropriately adjusted.

REFERENCES

[1] A. Emadi, Y. J. Lee, and K. Rajashekara, "Power electronics and motor drives in electric, hybrid electric, and plug-in hybrid electric vehicles," *IEEE Trans. Ind. Electron.*, vol. 55, no. 6, pp. 2237–2245, Jun. 2008.

[2] S. I. Kim, S. Park, T. Park, J. Cho, W. Kim, and S. Lim, "Investigation and experimental verification of a novel spoke-type ferrite-magnet motor for electric-vehicle traction drive applications," *IEEE Trans. Ind. Electron.*, vol. 61, no. 10, pp. 5763–5770, Oct. 2014.

[3] E. Bostanci, M. Moallem, A. Parsapour, and B. Fahimi, "Opportunities and challenges of switched reluctance motor drives for electric propulsion: a comparative study," *IEEE Trans. Transp. Electrification*, vol. 3, no. 1, pp. 58–75, Mar. 2017.

[4] A. Haddoun, M. E. H. Benbouzid, D. Diallo, R. Abdessemed, J. Ghouili, and K. Srairi, "Modeling, analysis, and neural network control of an EV electrical differential," *IEEE Trans. Ind. Electron.*, vol. 55, no. 6, pp. 2286–2294, Jun. 2008.

[5] G. Pellegrino, A. Vagati, P. Guglielmi, and B. Boazzo, "Performance comparison between surface-mounted and interior PM motor drives for electric vehicle application," *IEEE Trans. Ind. Electron.*, vol. 59, no. 2, pp. 803–811, Feb. 2012.

[6] L. Dang, N. Bernard, N. Bracikowski, and G. Berthiau, "Design optimization with flux weakening of high-speed PMSM for electrical vehicle considering the driving cycle," *IEEE Trans. Ind. Electron.*, vol. 64, no. 12, pp. 9834–9843, Dec. 2017.

[7] G. Zhang, W. Hua, M. Cheng, and J. Liao, "Design and comparison of two six-phase hybrid-excited flux-switching machines for EV/HEV applications," *IEEE Trans. Ind. Electron.*, vol. 63, no. 1, pp. 481–493, Jan. 2016.

[8] Y. Gao, D. Li, R. Qu, X. Fan, J. Li, and H. Ding, "A novel hybrid excitation flux reversal machine for electric vehicle propulsion," *IEEE Trans. Veh. Technol.*, vol. 67, no. 1, pp. 171–182, Jan. 2018.

[9] Z. Q. Zhu, N. Pothi, P. L. Xu, and Y. Ren, "Uncontrolled generator fault protection of novel hybrid-excited doubly salient synchronous machines with field excitation current control," *IEEE Trans. Ind. Appl.*, vol. 55, no. 4, pp. 3598–3606, Jul./Aug. 2019.

[10] P. B. Reddy, A. M. El-Refaie, K.-K. Huh, J. K. Tangudu, and T. M. Jahns, "Comparison of interior and surface PM machines equipped with fractional-slot concentrated windings for hybrid traction applications," *IEEE Trans. Energy Convers.*, vol. 27, no. 3, pp. 593–602, Sep. 2012.

[11] J. Nerg, M. Rilla, V. Ruuskanen, J. Pyrhonen, and S. Ruotsalainen, "Direct-driven interior magnet permanent-magnet synchronous motors for a full electric sports car," *IEEE Trans. Ind. Electron.*, vol. 61, no. 8, pp. 4286–4294, Aug. 2014.

[12] D. Golovanov, L. Papini, D. Gerada, Z. Xu, and C. Gerada, "Multidomain optimization of high-power-density PM electrical machines for system architecture selection," *IEEE Trans. Ind. Electron.*, vol. 65, no. 7, pp. 5302–5312, Jul. 2018.

[13] S. Niu, S. L. Ho, and W. N. Fu, "A novel direct-drive dual-structure permanent magnet machine," *IEEE Trans. Magn.*, vol. 46, no. 6, pp. 2036–2039, Jun. 2010.

[14] Y. Ma, T. W. Ching, W. N. Fu, and S. Niu, "Multi-objective optimization of a direct-drive dual-structure permanent magnet machine," *IEEE Trans. Magn.*, vol. 55, no. 10, Oct. 2019, Art. no. 7501704.

[15] W. Gul, Q. Gao, and W. Lenwari, "Optimal design of a 5-MW double-stator single-rotor PMSG for offshore direct drive wind turbines," *IEEE Trans. Ind. Appl.*, vol. 56, no. 1, pp. 216–225, Jan./Feb. 2020.

[16] W. Zhao, D. Chen, T. A. Lipo, and B.-I. Kwon, "Dual airgap stator- and rotor-permanent magnet machines with spoke-type configurations using phase-group concentrated coil windings," *IEEE Trans. Ind. Appl.*, vol. 53, no. 4, pp. 3327–3335, Jul./Aug. 2017.

[17] H. Chen, X. Liu, J. Zhao, and N. A. O. Demerdash, "Magnetic-coupling characteristics investigation of a dual-rotor fault-tolerant PMSM," *IEEE Trans. Energy Convers.*, vol. 33, no. 1, pp. 362–372, Mar. 2018.

[18] Y. Li, D. Bobba, and B. Sarlioglu, "Design and optimization of a novel dual-rotor hybrid PM machine for traction application," *IEEE Trans. Ind. Electron.*, vol. 65, no. 2, pp. 1762–1771, Feb. 2018.

[19] J. H. J. Potgieter and M. J. Kamper, "Double PM-rotor, toothed, toroidal-winding wind generator: a comparison with conventional winding direct-drive PM wind generators over a wide power range," *IEEE Trans. Ind. Appl.*, vol. 52, no. 4, pp. 2881–2891, Jul./Aug. 2016.

[20] S. C. Oh and A. Emadi, "Test and simulation of axial flux-motor characteristics for hybrid electric vehicles," *IEEE Trans. Veh. Technol.*, vol. 53, no. 3, pp. 912–919, May 2004.

[21] W. Zhao, T. A. Lipo, and B. I. Kwon, "Comparative study on novel dual stator radial flux and axial flux permanent magnet motors with ferrite magnets for traction application," *IEEE Trans. Magn.*, vol. 50, no. 11, Nov. 2014, Art. no. 8104404.

[22] Y. Lu *et al.*, "Six-phase double-stator inner-rotor axial flux PM machines with novel detached winding," *IEEE Trans. Ind. Appl.*, vol. 53, no. 3, pp. 1931–1941, May/Jun. 2017.

[23] Y. Lu, J. Li, R. Qu, D. Ye, and H. Lu, "Electromagnetic force and vibration study on axial flux permanent magnet synchronous machines

with dual three-phase windings," *IEEE Trans. Ind. Electron.*, vol. 67, no. 1, pp. 115–125, Jan. 2020.
[24] A. Mahmoudi, S. Kahourzade, N. A. Rahim, W. P. Hew, and M. N. Uddin, "Design, analysis, and prototyping of a novel-structured solid-rotor-ringed line-start axial-flux permanent-magnet motor," *IEEE Trans. Ind. Electron.*, vol. 61, no. 4, pp. 1722–1734, Apr. 2014.
[25] W. Geng and Z. Zhang, "Analysis and implementation of new ironless stator axial-flux permanent magnet machine with concentrated nonoverlapping windings," *IEEE Trans. Energy Convers.*, vol. 33, no. 3, pp. 1274–1284, Sep. 2018.
[26] R. Huang, C. Liu, Z. Song, and H. Zhao, "Design and analysis of a novel axial-radial flux permanent magnet machine with Halbach-array permanent magnets," *Energies*, vol. 14, no. 12, p. 3639, Jun. 2021.
[27] Hunstable, Fred E. "Multi-tunnel electric motor/generator." U.S. Patent No. 9,729,016. Aug. 2017.
[28] C. Liu, G. Lei, T. Wang, Y. Guo, Y. Wang, and J. Zhu, "Comparative study of small electrical machines with soft magnetic composite cores," *IEEE Trans. Ind. Electron.*, vol. 64, no. 2, pp. 1049–1060, Feb. 2017.
[29] W. Xu, N. Duan, S. Wang, Y. Guo, and J. Zhu, "Modeling and measurement of magnetic hysteresis of soft magnetic composite materials under different magnetizations," *IEEE Trans. Ind. Electron.*, vol. 64, no. 3, pp. 2459–2467, Mar. 2017.
[30] C. W. Ayers, J. S. Hsu, L. D. Marlino, C. W. Miller, G. W. Ott, and C. B. Oland, "Evaluation of 2004 Toyota Prius hybrid electric drive system interim report," ORNL/TM-2004/247, Nov. 2004.
[31] T. A. Burress *et al*., "Evaluation of the 2007 Toyota Camry hybrid synergy drive system," ORNL/TM-2007/190, Apr. 2008.
[32] H. Chen, X. Liu, N. A. O. Demerdash, A. M. EL-Refaie, Z. Chen, and J. He, "Computationally efficient optimization of a five-phase flux-switching PM machine under different operating conditions," *IEEE Trans. Veh. Technol.*, vol. 68, no. 7, pp. 6495–6508, Jul. 2019.
[33] H. Li, Z. Q. Zhu, and H. Hua, "Comparative analysis of flux reversal permanent magnet machines with toroidal and concentrated windings," *IEEE Trans. Ind. Electron.*, vol. 67, no. 7, pp. 5278–5290, Jul. 2020.
[34] A. Bharadwaj, *Electrician Trade Theory*. Abhishek Publications, 2020.
[35] K. R. Shah, "Measurement of stray load loss of d.c. machines," (1965). Master Theses. 6693.
[36] L. Del Ferraro, F. Caricchi, and F. G. Capponi, "Analysis and comparison of a speed-dependant and a torque-dependant mechanical device for wide constant power speed range in AFPM starter/alternators," *IEEE Trans. Power Electron.*, vol. 21, no. 3, pp. 720–729, May 2006.
[37] J. S. Hsu, S. C. Nelson, P. A. Jallouk, C. W. Ayers, R. H. Wiles, S. L. Campbell, C. L. Coomer, K. T. Lowe, and T. A. Burress, "Report on Toyota Prius motor thermal management," ORNL/TM-2005/33, Feb. 2005.
[38] X. Chen, J. Wang, A. Griffo, and A. Spagnolo, "Thermal modeling of hollow conductors for direct cooling of electrical machines," *IEEE Trans. Ind. Electron.*, vol. 67, no. 2, pp. 895–905, Feb. 2020.
[39] X. Fan, R. Qu, J. Li, D. Li, B. Zhang, and C. Wang, "Ventilation and thermal improvement of radial forced air-cooled FSCW permanent magnet synchronous wind generators," *IEEE Trans. Ind. Appl.*, vol. 53, no. 4, pp. 3447–3456, Jul. 2017.

Hao Chen (Member, IEEE**)** received the B.Sc. degree in electrical engineering from the School of Electrical Engineering, Beijing Jiaotong University, Beijing, China, in 2012, and the Ph.D. degree in control science and engineering from the School of Automation, Beijing Institute of Technology, Beijing, China, in 2019.

From 2016 to 2018, he was with the Department of Electrical and Computer Engineering, Marquette University, Milwaukee, WI, USA, as a Joint Ph.D. Student. He is currently a Postdoctoral Research Fellow with the School of Electrical and Electronic Engineering, Nanyang Technological University, Singapore.

His research interests include the design and optimization of electric machines, power electronic drives, and motor control.

Nabeel A. O. Demerdash (Life Fellow, IEEE) received the B.Sc.E.E. degree (distinction with first-class Hons.) in electrical engineering from Cairo University, Giza, Egypt, in 1964, and the M.S. and Ph.D. degrees in electrical engineering from the University of Pittsburgh, Pittsburgh, PA, USA, in 1967 and 1971, respectively.

From 1968 to 1972, he was a Development Engineer in the Large Rotating Apparatus Development Engineering Department, Westinghouse Electric Corporation, East Pittsburgh. From 1972 to 1983, he was an Assistant Professor, an Associate Professor, and then a Professor in the Department of Electrical Engineering, Virginia Polytechnic Institute and State University, Blacksburg, VA, USA. From 1983 to 1994, he was a Professor in the Department of Electrical and Computer Engineering, Clarkson University, Potsdam, NY, USA. Since 1994, he has been a Professor with the Department of Electrical and Computer Engineering, Marquette University, Milwaukee, WI, USA, where he was the Department Chair from 1994 to 1997. He is the Director of the SEMPEED Consortium at Marquette University. He is the author or co-author of more than 125 papers published in various IEEE TRANSACTIONS. His current research interests include power electronic applications to electric machines and drives, electromechanical propulsion and actuation, computational electromagnetics in machines and drives, and fault diagnostics and modeling of motor-drive systems.

Prof. Demerdash is a member of the Electric Machines Committee of the IEEE Industry Applications Society, the American Society of Engineering Education, Sigma Xi, and the Electromagnetics Academy. He has received the 1999 IEEE Nikola Tesla Technical Field Award for pioneering contributions to electric machine and drive system design using coupled finite-element and electrical network models. He has also received two 1994 Working Group Awards and two 1993 Prize Paper Awards from the IEEE Power and Energy Society (PES) and its Electric Machinery Committee, and a 2012 Prize Paper Award from the PES, as well as a 2012 Prize Paper Award from the IEEE Industry Applications Society Electric Machines Committee and the 2015 Marquette University Lawrence G. Haggerty Faculty Award for Research Excellence.

Ayman M. EL-Refaie (Fellow, IEEE) received the B.S and M.S degrees in electrical power engineering from Cairo University, Giza, Egypt, in 1995 and 1998, respectively. He received the M.S. and Ph.D. degrees in electrical engineering from the University of Wisconsin-Madison, Madison, WI, USA, in 2002 and 2005, respectively.

Between 2005 and 2016, he has been a Principal Engineer and a Project Leader with the Electrical Machines and Drives Lab at General Electric Global Research Center. Since January 2017, he joined Marquette University as the Werner Endowed Chair for Energy Sustainability. He has over 160 journal and conference publications. He has 48 issued US patents. At GE, he worked on several projects that involve the development of advanced electrical machines for various applications including aerospace, traction, wind, and water desalination. His research interests include electrical machines and drives.

Dr. EL-Refaie was the chair for the IEEE IAS Transportation Systems committee and an Associate Editor for the Electric Machines committee. He was a Technical Program Chair for the IEEE 2011 Energy Conversion Conference and Exposition (ECCE). He was the General Chair for ECCE 2014 and 2015 ECCE steering committee chair. He was the general chair of IEMDC 2019. He is the past chair of the IEEE IAS Industrial Power Conversion Systems Department and currently he is the IEEE Industry Applications Society Publications Department chair.

Youguang Guo (Senior member, IEEE) is currently a Professor with the School of Electrical and Data Engineering, University of Technology Sydney (UTS).

He received the B.E. degree from Huazhong University of Science and Technology (HUST), China in 1985, the M.E. degree from Zhejiang University, China in 1988, and the PhD degree from UTS, Australia in 2004, all in electrical engineering.

From 1988 to 1998, he was an associate lecturer/lecturer in the Department of Electric Power Engineering, HUST. From March 1998 to July 2008, he worked as visiting research fellow, PhD candidate, postdoctoral fellow and research fellow in the Centre for Electrical Machines and Power Electronics, Faculty of Engineering, UTS. Since 2008, he has been an academic with the Faculty of Engineering and Information Technology, UTS.

His research fields include measurement and modelling of magnetic properties of magnetic materials, electrical machine design and optimization, electric motor drives and control.

Wei Hua (Senior member, IEEE) received the B.Sc. and Ph.D. degrees in electrical engineering from Southeast University, Nanjing, China, in 2001 and 2007, respectively. From 2004 to 2005, he was with the Department of Electronics and Electrical Engineering, The University of Sheffield, U.K., as a Joint-Supervised Ph.D. Student.

Since 2007, he has been with Southeast University, where he is currently a Chief Professor of Southeast University and a Distinguished Professor of Jiangsu Province. From 2010, he has also worked with Yancheng Institute of New Energy Vehicles of Southeast University. He has co-authored over 150 technical papers. He holds 50 patents in his areas of interest. His teaching and research interests include design, analysis, and control of electrical machines, especially for PM brushless machines and switching reluctance machines, etc.

Christopher H. T. Lee (Senior member, IEEE) received the B.Eng. (Hons.) and Ph.D. degrees in electrical engineering from the Department of Electrical and Electronic Engineering, The University of Hong Kong, Pokfulam, Hong Kong, in 2009 and 2016, respectively.

He currently serves as an Assistant Professor with the School of Electrical and Electronic Engineering, Nanyang Technological University, Singapore, a Visiting Assistant Professor at Massachusetts Institute of Technology, Cambridge, MA, USA, and an Honorary Assistant Professor in his alma mater. His research interests include electric machines and drives, renewable energies, and electric vehicle technologies. In these areas, he has published one book, three book chapters, and about 70 referred papers.

Dr. Lee received many awards, including the Nanyang Assistant Professorship, the Li Ka Shing Prize (the best Ph.D. thesis prize) and Croucher Foundation Fellowship to support his postdoctoral research. He is also an Associate Editor of IEEE ACCESS and *IET Renewable Power Generation*.